Transport of superparamagnetic beads through a two-dimensional potential energy landscape

Mukarram A. Tahir,[1,*] Lu Gao,[1] Lawrence N. Virgin,[1] and Benjamin B. Yellen[1,2]

[1]*Duke University, Department of Mechanical Engineering and Materials Science, Center for Biologically Inspired Materials and Materials Systems (CBIMMS), Durham, North Carolina 27708, USA*

[2]*University of Michigan-Shanghai Jiao Tong Joint Institute, Shanghai Jiao Tong University, Shanghai 200040, People's Republic of China*

(Received 20 October 2010; revised manuscript received 9 May 2011; published 26 July 2011)

The nonlinear dynamic behavior of superparamagnetic beads transported through a two-dimensional potential energy landscape is explored empirically and through numerical simulation. The beads are driven through a periodic array of micromagnets by an external rotating field oriented at an angle θ relative to the magnetization direction of the substrate. The bead's motion was highly sensitive to the angle of the driving field near critical angles and to various system parameters, including bead size, rotation frequency, and substrate pole density. Our results suggest the possibility of using this behavior in a highly discriminative colloidal separation system, in which two different bead types can be tuned to move in orthogonal directions.

DOI: 10.1103/PhysRevE.84.011403 PACS number(s): 82.70.Dd, 05.45.−a, 64.75.Xc

I. INTRODUCTION

The propagation of magnetic particles through a micromagnet lattice in time-modulated external fields is a subset of a broad class of systems that describe the behavior of particles of various kinds moving through potential energy landscapes. Some physical examples include electron transport in a lattice of scatterers, [1] driven charge density waves, [2] driven vortex lattices, [3] and colloidal transport [4–18] by electric, magnetic, or optical fields. These systems are physically intriguing due to their rich nonlinear synchronization behavior (often given unusual names such as Devil's staircases, Arnold tongues, and Farey trees) and different regimes of periodic entrainment of the particle relative to the underlying lattice. The ability to precisely tune the synchronization of driven objects has been exploited in a number of applications, which at their root have the same common goal of separating particles (e.g., electrons, flux vortices, and colloidal particles) in order to dynamicaly control the flow of information, material, or energy.

Colloidal systems are convenient experimental models to study these dynamic systems because the synchronization processes can be observed at the single-particle level. In particular, the transition between phase-locked and phase-slipping states has been observed in the magnetophoretic, [4–11] dielectrophoretic, [12] and optophoretic [13–18] transport of beads through a periodic lattice. During phase-locked motion, the bead is trapped in a potential energy minima and moves through the lattice at a characteristic rate defined by the oscillator driving frequency. During phase-slipping motion, the bead can no longer remain in phase with the oscillator due to large external friction, resulting in a range of quasiperiodic and subharmonic motions that depend on the external damping conditions. By controlling the transition between these two states, highly discriminate separation between different colloidal species has been achieved based on minor differences in the particle size or its material properties. [4–6]

Two-dimensional (2D) motion of glass spheres flowing through an array of optical traps has been demonstrated by Grier and colleagues, [14] which revealed that the particle trajectories could be strongly influenced by the periodicity and strength of the optical lattice, tending to follow along preferred lattice directions at different driving angles. Motivated by the interesting results and potential for colloidal fractionation, here we investigate the motion of superparamagnetic beads at different driving angles relative to the magnetization direction of the substrate. Through a combination of numerical simulation and experiment, we demonstrate that the magnetophoretic system has the potential to achieve extremely high separation resolution between different bead types. Briefly, our results suggest that it is possible to cause two different colloidal species to move at right angles, which can have a tremendous impact in life sciences and lab-on-a-chip applications.

The rest of the manuscript is organized as follows. In Sec. II, we derive the equations of motion for the beads and describe our numerical simulation methods. In Sec. III, we describe the experimental apparatus that was used to observe the various dynamics predicted by simulations. In Sec. IV, we discuss the results obtained from simulations and experiments and their application to colloidal separation, and conclude in Sec. V with an overview of future work.

II. COMPUTATIONAL METHODS

Our experimental model consists of an array of micromagnets all uniformly magnetized along the x axis according to the schematic in Fig. 1. To first-order approximation, the substrate field distribution can be modeled as a 2D array of point poles with positive and negative charges denoting the north and south poles of the magnets. The pole density for an array of Dirac delta functions is modeled through Fourier series as

$$\sigma(x,y) = \lambda \sum_{n=1}^{\infty} \sum_{m=-\infty}^{\infty} \left[\cos\left(\frac{2\pi}{d} nx\right) - \cos\left(\frac{2\pi}{d} nx - \frac{2\pi n d_{\mathrm{mag}}}{d}\right) \right] \cos\left(\frac{2\pi}{d} my\right), \tag{1}$$

where d_{mag} is the diameter of the magnet, d is the lattice period, and λ is the effective charge density of the substrate determined through matching with experiment. Through separation of

*mukarram.tahir@duke.edu

variables and matching the boundary conditions of (1), the fields produced by the substrate are given by

$$\vec{H}^{\text{sub}} = \left\{ \begin{array}{c} \lambda \sum_{n=1}^{\infty} \sum_{m=-\infty}^{\infty} \frac{n}{\sqrt{m^2+n^2}} \left[\sin\left(\frac{2\pi}{d} nx\right) - \sin\left(\frac{2\pi}{d} nx - \frac{2\pi n d_{\text{mag}}}{d}\right) \right] \cos\left(\frac{2\pi}{d} my\right) e^{-\frac{2\pi}{d}\sqrt{m^2+n^2}z} \\ \lambda \sum_{n=1}^{\infty} \sum_{m=-\infty}^{\infty} \frac{m}{\sqrt{m^2+n^2}} \left[\cos\left(\frac{2\pi}{d} nx\right) - \cos\left(\frac{2\pi}{d} nx - \frac{2\pi n d_{\text{mag}}}{d}\right) \right] \sin\left(\frac{2\pi}{d} my\right) e^{-\frac{2\pi}{d}\sqrt{m^2+n^2}z} \\ \lambda \sum_{n=1}^{\infty} \sum_{m=-\infty}^{\infty} \left[\cos\left(\frac{2\pi}{d} nx\right) - \cos\left(\frac{2\pi}{d} nx - \frac{2\pi n d_{\text{mag}}}{d}\right) \right] \cos\left(\frac{2\pi}{d} my\right) e^{-\frac{2\pi}{d}\sqrt{m^2+n^2}z} \end{array} \right\}. \quad (2)$$

The particles are driven through the micromagnet lattice with a uniform external field of magnitude H^{ext} that is rotating at a frequency ω and applied at an orientation θ relative to the magnetization of the micromagnets (i.e., track magnetization). The external fields are thus represented as

$$\vec{H}^{\text{ext}} = H^{\text{ext}} \begin{bmatrix} \cos\omega t \cos\theta \\ \cos\omega t \sin\theta \\ \sin\omega t \end{bmatrix}. \quad (3)$$

Using the force equation for a point dipole in a magnetic field gradient, $\mathbf{F} = \mu_0 (\mathbf{m} \cdot \nabla) \mathbf{H}$, with $\mathbf{m} = \bar{\chi} V \mathbf{H}$ and assuming that $H^{\text{ext}} \gg H^{\text{sub}}$, we can determine the lateral magnetic force on the beads to be

$$F_x = F_{\text{mag}} \sum_{n=1}^{\infty} \sum_{m=-\infty}^{\infty} \left[\frac{n^2 g_n g_m \alpha_{n,m}}{\sqrt{m^2+n^2}} \cos\omega t \cos\theta - \frac{nm f_n f_m \alpha_{n,m}}{\sqrt{m^2+n^2}} \cos\omega t \sin\theta - n f_n g_m \alpha_{n,m} \sin\omega t \right], \quad (4)$$

$$F_y = F_{\text{mag}} \sum_{n=1}^{\infty} \sum_{m=-\infty}^{\infty} \left[-\frac{nm f_n f_m \alpha_{n,m}}{\sqrt{m^2+n^2}} \cos\omega t \cos\theta + \frac{m^2 g_n g_m \alpha_{n,m}}{\sqrt{m^2+n^2}} \cos\omega t \sin\theta - m g_n f_m \alpha_{n,m} \sin\omega t \right], \quad (5)$$

where the following substitutions are made to simplify the notation:

$$F_{\text{mag}} = \frac{2\mu_0 \bar{\chi} \lambda \pi V H^{\text{ext}}}{d}, \quad (6a)$$

$$g_n = \left[\cos\left(\frac{2\pi n}{d} x\right) - \cos\left(\frac{2\pi n}{d}(x - d_{\text{mag}})\right) \right], \quad (6b)$$

$$f_n = \left[\sin\left(\frac{2\pi n}{d} x\right) - \sin\left(\frac{2\pi n}{d}(x - d_{\text{mag}})\right) \right], \quad (6c)$$

$$g_m = \cos\left(\frac{2\pi m}{d} y\right), \quad (6d)$$

$$f_m = \sin\left(\frac{2\pi m}{d} y\right), \quad (6e)$$

$$\alpha_{n,m} = e^{-\frac{2\pi}{d}\sqrt{m^2+n^2}z}. \quad (6f)$$

In the above equations, μ_0 represents the magnetic permeability of free space, $\bar{\chi} = 3\chi/(\chi + 3)$ is the bead's magnetic volume susceptibility corrected for its spherical shape, and V is the volume of the bead.

For simplicity, we have ignored the force in the z direction because the force is usually negative (i.e., attractive toward the substrate) and the height of the bead was not found to change dramatically during our simulations. Thus, the forcing dynamics are assumed to be wholly accounted for using the lateral forces F_x and F_y to describe the translation of the beads across the substrate. In order to simplify the analysis, Brownian motion was ignored in our calculations, which is reasonable for colloidal particles larger than a few microns that are exposed to strong external forces. We also verified through numerical simulations that the inertial terms were negligible, which is quite reasonable for low Reynold's number systems; thus the equations of particle motion in the overdamped limit were expressed as

$$\frac{dx}{dt} = \frac{F_x}{6\pi\eta a}, \quad (7a)$$

$$\frac{dy}{dt} = \frac{F_y}{6\pi\eta a}. \quad (7b)$$

Here, a is the bead radius, and η represents the dynamic viscosity of water. All simulations were performed in the PYTHON programming language, using Euler's method for numerical integration; however, we verified that the simulations did not change when the equations of motion were programmed in different software packages and using different integration techniques. A timestep of 1/100th of a cycle was sufficient for numerical stability, and the average θ^* was determined through the inverse tangent of the ratio of magnets traveled along the x and y directions after 200 driving cycles. To ensure that transients were excluded from the presented results, we initialized our simulations for 200 cycles before running an additional 200 cycles, from which the end-to-end θ^* values were determined. We verified the accuracy of the Euler simulation method against other numerical methods, including fourth-order Runge-Kutta integration as well as adaptive timestep implemented in Mathematica's NDSolve routine. All simulations yielded practically indistinguishable results, and the overarching trends and key transition points in the computed θ^* versus θ relationships were insensitive to the choice of solution method for a sufficiently refined timestep.

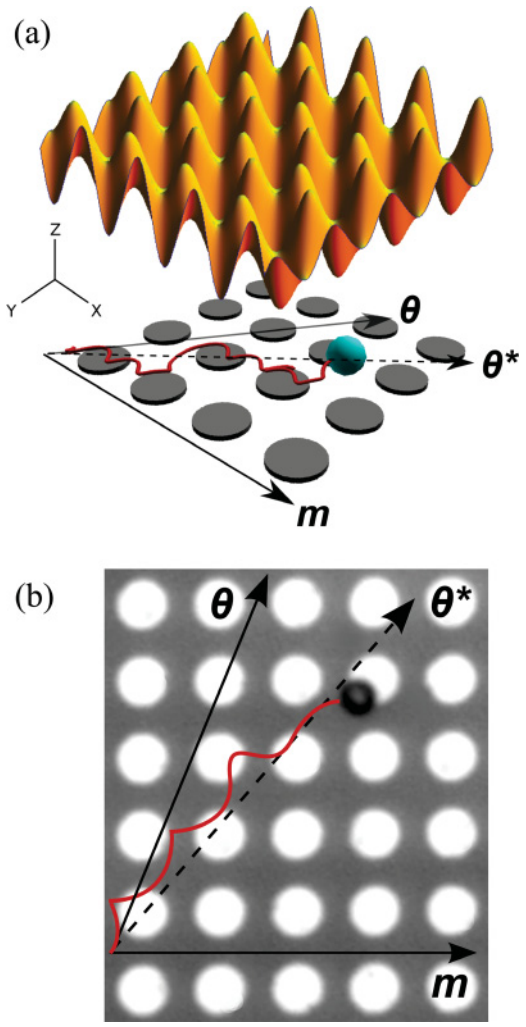

FIG. 1. (Color online) (a) The periodic potential energy landscape produced by an array of micromagnets is plotted above a schematic of the experimental system. The (blue) sphere represents the superparamagnetic bead, and the trailing (solid red) line denotes one of the expected trajectories under a rotating field applied at an angle θ relative to the track magnetization **m**. The average angle of motion θ^* is different from θ. (b) An experimental image depicting a 1.35 μm radius bead moving across an array of magnets, where the angles θ and θ^* are illustrated by arrows, and experimental trajectory by the trailing (solid red) line.

III. MATERIALS AND METHODS

In our experimental work, we used substrates composed of a square lattice of circular 4.9-μm micromagnets with 8.0-μm periodicity. The external rotating field apparatus has been described in previous work. [4] Originally we fabricated the micromagnets using conventional photolithographic lift-off process [19] using single-layer Co; however, due to the low coercivity of thin Co films, we had to resort to more complex Co-Pd multilayer magnets that could better resist remagnetization against the in-plane external fields oriented along the y direction. Co-Pd multilayers have both high coercivity and high remnant magnetization, which allow the track magnetization to remain fixed along the x direction even in the presence of a field component in the y direction. The data in Fig. 3 clearly show the effect of substrate remagnetization.

Although the optimal thicknesses for high coercivity reported in the literature [20] are 0.9 nm/0.28 nm for Pd/Co multilayers, limitations of our evaporation equipment (CHA Industries Solution E-Beam) allowed us to deposit 5-nm alternating layers for both Co and Pd without running into issues such as noncontinuous film deposition and inconsistent layer depths. Using a ferrofluid bitter decoration process, we found that the Co-Pd multilayers had a higher coercivity (remagnetizing above 50 Oe), whereas the single 50-nm-thick Co layer remagnetized at a lower field around 20–30 Oe.

We chose a magnetic field strength of 15 Oe for all experiments in order to maintain the integrity of the substrates' magnetization while allowing for adequate motion of the magnetic beads. To vary the orientation of the field, we constructed a rotational stage capable of $\sim 1^\circ$ accuracy in the field orientation. All experiments used 1.35-μm radius superparamagnetic beads (Invitrogen M-270 Dynabeads), which are convenient due to their high monodispersity in size and magnetization. To reduce adhesion with the substrate, the beads were washed and coated with Bovine Serum Albumin. The beads were diluted, dispersed in water, and then placed in a fluid well using a 100-μm insert layer (Invitrogen SecureSeal spacers) to reduce hydrodynamic friction from the top surface. An external rotating field at 0.5 Hz was applied to the system, leading to particle motion on the order of a few microns per second. Video capture and bead tracking were achieved with SimplePCI software and ImagePro interfaced with a Leica DMLM microscope. The video tracking speed was maintained at 4.3 frames per second in all experiments, and the camera exposure time was 2 milliseconds. Our camera has a pixel size of 290 nm, allowing for high-resolution trajectory analysis relative to the length scale of the micromagnet. Although this low tracking speed did not capture the fine details of the beads' motion, it was necessary for taking sufficiently long movies (a minute and longer) that could capture the long time average of the bead's trajectory. Care was taken to restrict our measurements to beads that were sufficiently isolated from surrounding ones, in order to evaluate the particle dynamics without interparticle interaction. The mean and standard deviations presented in Fig. 3 represent averages over five beads' trajectories. Though the motion was more or less uniform for all beads, we selected for measurements only those that had moved continuously for at least 20 magnets.

IV. RESULTS AND DISCUSSION

A comparison between the predicted and experimental trajectories is provided in Fig. 2 for different driving angles but constant driving frequency of 0.5 Hz. Qualitatively, the agreement between theory and experiment is reasonably good, evidenced by the highly visible hopping motion of the bead from one magnet to the next. Clearly, the experimental motion is more muted in terms of the actual trajectory, which may have resulted from surface adhesion and other subtrate friction effects that were not accounted for in our model. When the external field is oriented at 0° or 90° relative to the track magnetization, the beads move colinearly in the direction of the driving angle. For all other driving angles, there is

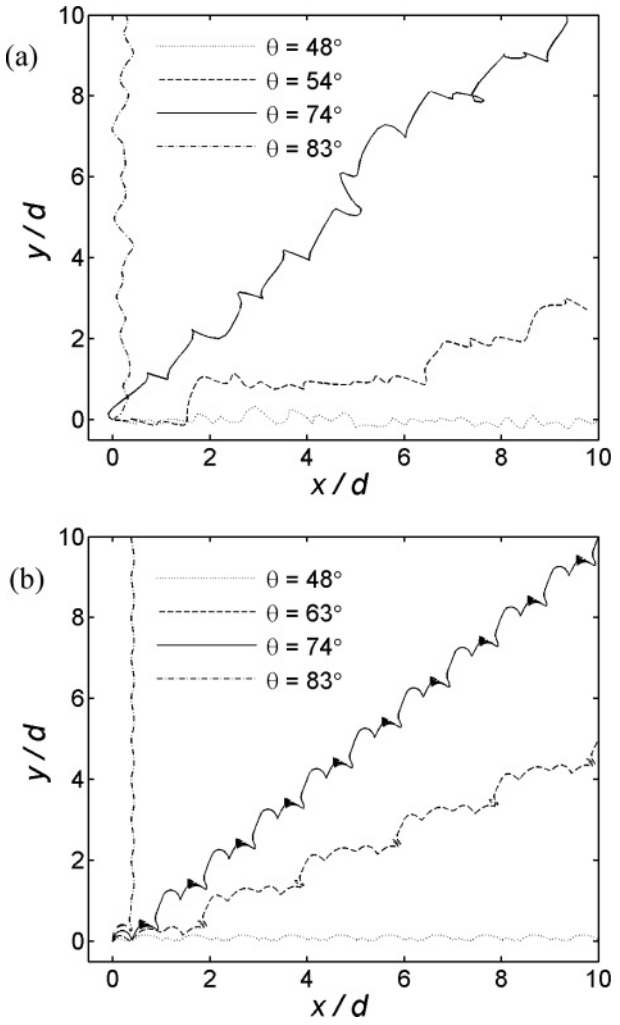

FIG. 2. Comparison between (a) experiment, and (b) simulation of characteristic trajectories exhibited by beads of radius 1.35 μm in an external field of 15 Oe, corresponding to $\lambda = 1.5$ Oe. The experimental data were obtained using the Co-Pd substrates.

a pronounced difference between θ and θ^*. For low driving angles, $\theta^* < \theta$, which results from the bead attempting to following the track direction while the driving field is pushing the bead away toward another adjacent track. For very high driving angles, the opposite occurs, i.e., $\theta^* > \theta$, in which case the bead prefers to follow a trajectory orthogonal to the track direction. Theory and simulation agreed reasonably well when the substrate magnetization λ is assumed to be 1.5 Oe. See Ref. [21] for a video depicting that motion of a sample of beads for the angles included in Fig. 2(a).

Experimental results for θ^* versus θ are provided in Fig. 3 to demonstrate how substrate remagnetization affects the bead trajectories. For single-layer Co, the preferred direction of transport clearly shifts at $\theta = 45^\circ$, which is consistent with the expected behavior of soft-magnetic material, where the easy axis becomes the 1,1 line in a 2D analogy to 3D crystallographic planes. The same results are observed for many driving frequencies, field strengths, and micromagnet thicknesses. For Co-Pd multilayers, the transition of bead motion away from the x direction (i.e. 1,0 line) is observed at much higher angles, e.g., $\theta > 60^\circ$. Moreover, the field strength,

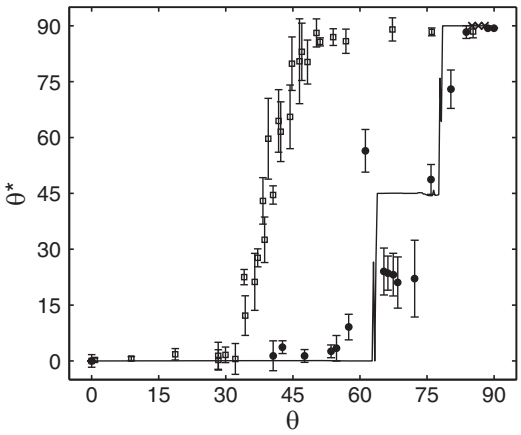

FIG. 3. Comparison between experiment and simulation of relationship between θ^* and θ (presented in degrees). The hollow squares and solid circles represent the bead trajectories on single-layer Co substrates and Co-Pd multilayers, respectively. Closed orbits are indictated as $\times$, which were observed only in simulations above 85° using the present system parameters.

driving frequency, and other control parameters lead to highly tunable bead trajectories that enable the design of a better separation system. Results from simulations using $\lambda = 1.5$ Oe were found to match the experimental data with regard to the key transition angles; however, the intermediate kinetic state of $\theta^* = 45^\circ$ was observed only rarely in experiments. We speculate that there are two likely causes of this discrepancy. First, the micromagnets are 5 μm in diameter and thus are likely to have multiple magnetic domains; furthermore even if they were single domain, the pole density of the micromagnets will still be distributed around the circumference of the magnet and cannot be represented exactly as an array of point charges. However, for the sake of deriving analytically tractable equations that could enable long time simulations, we resorted to the assumption of a point charge array. A second source discrepancy may be due to the possibility that the track magnetization could have tilted slightly along the y direction during our experiments. These two effects are not easy to include in simulations and would likely have contributed different types of errors, so for convenience we present the numerical simulations of a point charge array exclusively.

In order to explore the parameter space, we systematically varied all the control parameters, including driving frequency, field strength, and bead size. In Fig. 4 we present graphical relationships for the effect of substrate magnetization on the bead trajectories, and an additional phase diagram of θ^* versus θ is also provided in Fig. 4(d) in order to depict the general trends. Generally, as λ is increased, the transition of the bead's motion from the 1,0 to the 0,1 direction becomes sharper, and the range of angles for which different kinetic modes is observed also decreases. This switching behavior was not often observed in our experimental data for both Co and Co-Pd substrates, and we were surprised to see such erratic behavior in the velocity transition in our numerical simulations of the system. However, there is some experimental evidence that potentially large and abrupt changes in the direction of the bead's motion may occur near certain critical driving angles (see, e.g., the Co-Pd data near 60°) Originally, we

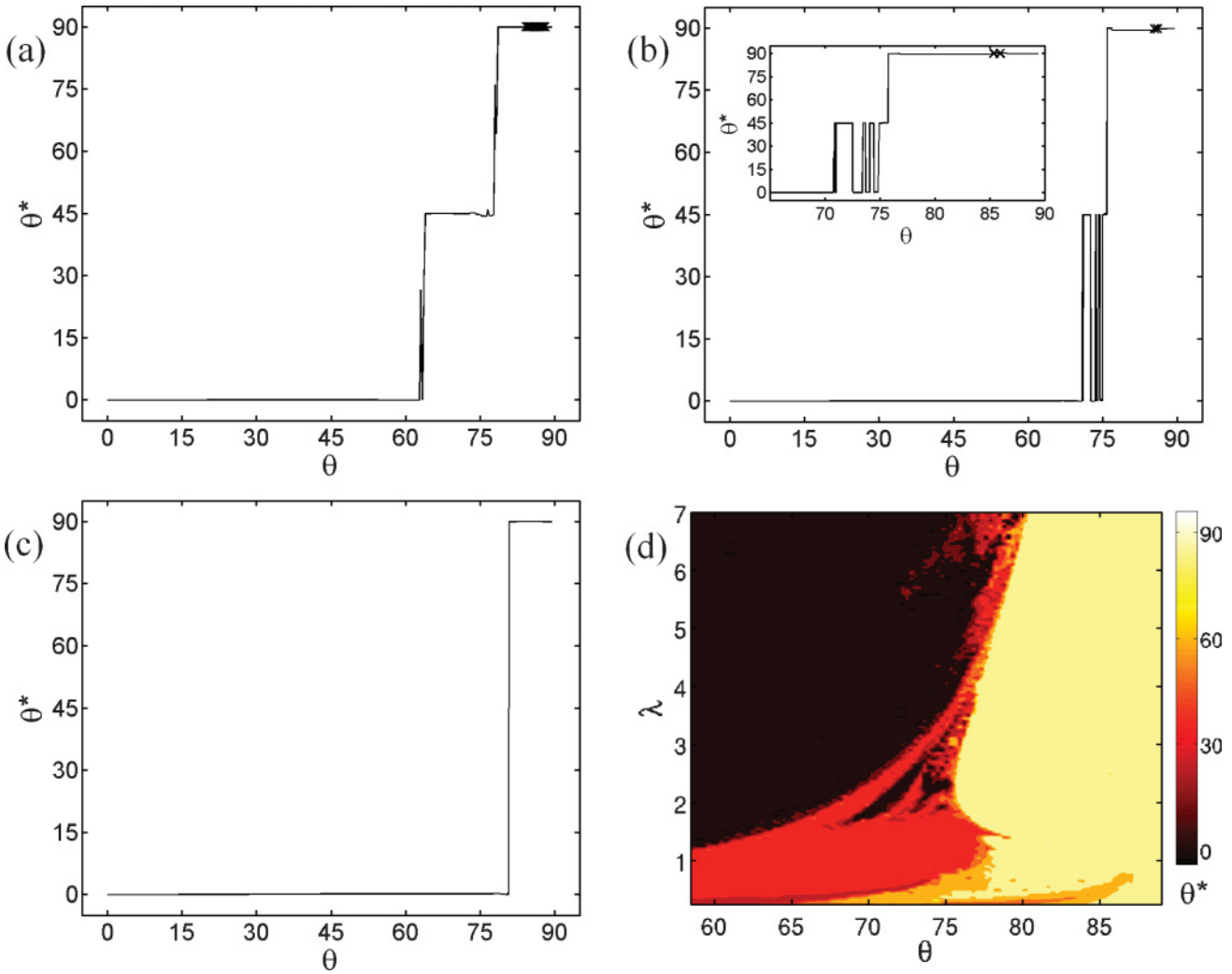

FIG. 4. (Color online) θ^* vs θ (in degrees) is plotted for various values of λ: (a) $\lambda = 1.5$ Oe, (b) $\lambda = 2.5$ Oe, (c) $\lambda = 7.5$ Oe. Closed orbits are indictated with $\times$, which were discovered only for certain initial conditions. (d) A phase diagram depicts the results for λ ranging between 0.25 and 7.0 Oe, with fixed 1.35 μm bead radius and 0.5 Hz driving frequency. The progression from black to red to yellow corresponds the abrupt switching primarily between primarily three states $\theta^* = 0^\circ$, 45°, and 90°. The intermediary states of $\theta^* = 30^\circ$ and 60° were sometimes observed, though rarely.

thought the nonintuitive simulation results were caused by numerical error; however, the same effect was observed regardless of the timestep, number of magnets traveled, or the type of integrator, e.g., Runge-Kutta, Euler difference, and the adaptive integration techniques built into Mathematica packages. We confirmed the same behavior occurred when inertial terms were included, as well as when the static forcing terms of the substrate were included in the equations of motion. [5] The phase plot in Fig. 4(d) demonstrates the reentrant transitions in the angle-driven bead transport at low driving frequencies. Note that the distinct colors on the plot representing unique regimes predominantly occurred near 0°, 45°, and 90°.

The transition angles of the switching behavior were predominantly independent of the initial conditions. For each driving angle, we tested 100 initial conditions (a 10×10 grid spanning one unit magnet cell) and found that for nearly all angles the steady-state trajectories were identical. Only in the vicinity of high driving angles ($\theta > 75^\circ$) did we observe a dependence on initial conditions, in which we found that for some initial conditions the beads were trapped in a closed orbit. This trapped state is depicted by using "x" markers for the θ^* data in Figs. 3–6. We observe that the beads in this state were dynamically trapped in local potential energy minima and could not escape. Video in Ref. [21] illustrates this trapping effect, which occurs only for certain initial conditions using the system parameters $\theta = 88^\circ$, a bead radius of 1.35 μm, a driving frequency of 0.5 Hz, and a substrate magnetization of 1.5 Oe. On the other hand, for a different set of initial conditions and using the same system parameters, an open orbit is produced. For other areas of the mobility spectrum, the jitter behavior observed in simulations remains a mystery. While these effects may be unexpected, our simulations indicate that the jitter in the switching behavior is not a numerical artifact and is not sensitive to initial conditions, except in the cases where closed orbits are produced instead of open orbits.

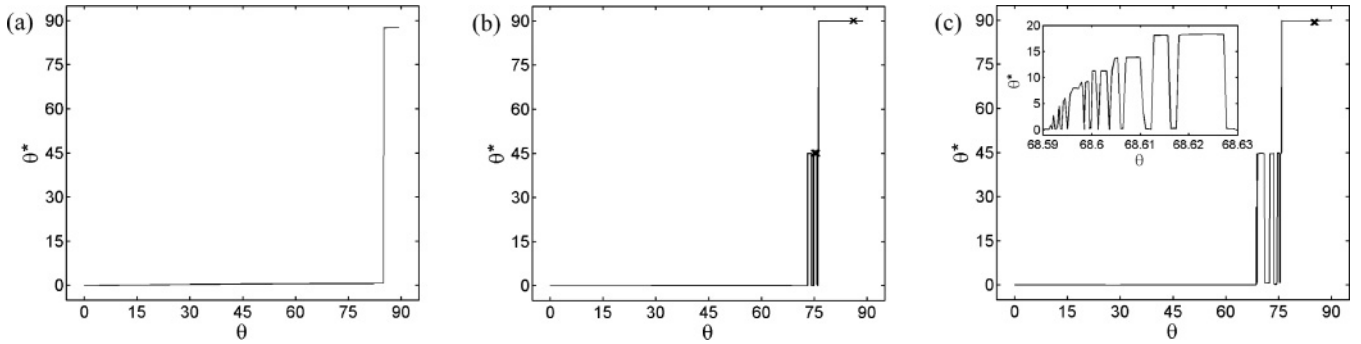

FIG. 5. Plots for simulation of relationship between θ^* and θ (both in degrees) for various driving frequencies: (a) 0.3 Hz, (b) 0.5 Hz, and (c) 0.7 Hz. Note that $\lambda = 3.0$ Oe in this case. Closed orbits are indictated with $\times$.

In Figs. 5 and 6, we present the effects of driving frequency and bead size on the resultant bead trajectories. When the driving frequency is increased, the transition from motion along the 1, 0 to the 0, 1 direction shifts to higher critical angles, and it also increases the prevlance of switching behavior within the θ^* versus θ relationship. For the particular case of f_{ext}= 0.7 Hz, we provide an inset within Fig. 5(c) to show a close-up view of the jitter behavior in the bead trajectory simulations. Fig. 6 represents the effect of three different bead radii on the resulting trajectories, and we provide an additional phase diagram of θ^* versus θ in Fig. 6(d), which graphically depicts the general trends as a function of the bead radius. Since larger beads will move along the track magnetization at higher driving angles than small beads, this finding suggests the ability to achieve 2D bead separation by adjusting the driving angle to a critical threshold. For example, if an 80° driving angle is used, the 1.35-μm radius beads will move along the y direction while the 2.0 and 3.0-μm

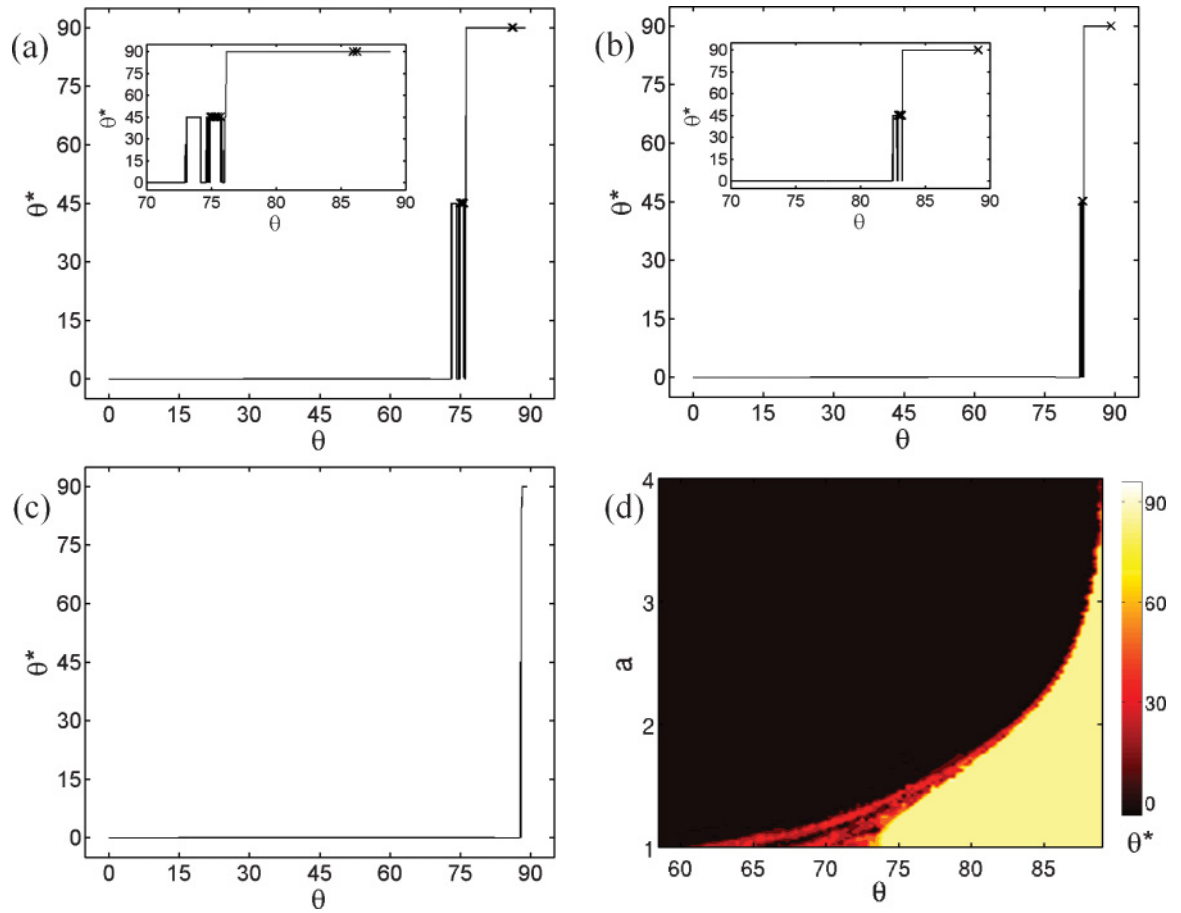

FIG. 6. (Color online) θ^* vs θ (in degrees) is plotted for bead radius, a, of 1.35 μm, (b) 2.0 μm, and (c) 3.0 μm. Closed orbits are indictated with $\times$. (d) A phase diagram depicting the velocity spectrum for bead sizes ranging between 1.0 and 4.0 μm, with $\lambda = 3.0$ Oe and driving frequency being 0.5 Hz. For these conditions, the bead trajectory switches between predominantly two states $\theta^* = 0°$ or 90°, respectively.

radius beads will move along the x direction. A different set of angles can separate the 2.0- and 3.0-μm radius beads in a similar manner. Figure 6(d) is further illustrative of the system's potential to induce divergent transport in beads of varying radii, with field orientation being the only control parameter. The system allows particles of specific radii to be successively isolated from a dispersion, leading to an efficient separation mechanism. Note that the critical angle dependence on bead size results from an amalgamation of effects that include differences in the volume [exhibited by the parameter V in Eq. (6a)], vertical location of the bead center [parameter z in Eq. (6f)], and viscous drag coefficient [hydrodynamic size parameter a in Eq. (7)]. This analysis suggests that orthogonal motion can also be induced in two different sets of identical beads that differ only in the type of nonmagnetic physical coating (e.g., a protein, virus, bacteria monolayer), which would alter the bead's hydrodynamic size and its vertical location above the substrate in Eqs. (7) and (6f), respectively. Due to the small size of proteins, this effect would not be observable for micron-sized beads; however, it could become a useful separation approach when scaled into the submicron regime.

Compared with alternative linear magnetic separation techniques, such as field flow fractionation, which can also sort particles based on size [22–24] and separate polymers [25], the magnetic separation technique presented here utilizes nonlinear synchronization behavior, which can dramatically improve the separation resolution. Conventional field-flow fractionation method works by imposition of a field gradient orthogonal to a channel through which samples are flowed at various speeds. [26] Due to differences in material properties such as particle size or hydrodynamic diameter, various constituents of the sample are driven to exit the channel at different times or at different positions. In this inherently linear system, the separation resolution scales with the square of the bead radius, since magnetic force scales with volume and viscous drag scales with radius. On the other hand, our method uses nonlinear dynamics to move beads along potentially orthogonal directions under the same operating conditions. Thus, it is possible to tune this device to achieve highly discriminative separation resolution between different species, leading to greater efficiency and smaller devices.

Despite our recent progress, there are some issues that require future optimization. For example, when the substrate magnetization becomes too large (i.e., very high λ), then the beads become locally trapped in closed orbits at high driving angles, θ. Work is ongoing to develop improved experiments that can achieve the correct λ and ω that will enable practical applications of this approach in colloidal separation in microenvironments.

V. CONCLUSIONS

In this work we explored the fascinating dynamics of superparamagnetic beads transported in a 2D potential landscape as a function of the driving angle between an external rotating field and the track magnetization. We observed that the beads exhibit interesting locking modes and different 2D trajectories that can be adjusted with the driving angle. The bead trajectory is very sensitive to various experimental parameters such as driving frequency and bead size, which allows us to tune the system to cause beads to travel in orthogonal directions. This observation has important applications in magnetic separation, and our current efforts are focused on improving the micromagnet substrates to realize this separation system more efficiently.

[1] J. Wiersig and K.-H. Ahn, Phys. Rev. Lett. **87**, 026803 (2001).

[2] S. E. Brown, G. Mozurkewich, and G. Grüner, Phys. Rev. Lett. **52**, 2277 (1984).

[3] C. Reichhardt and F. Nori, Phys. Rev. Lett. **82**, 414 (1999).

[4] L. Gao, N. Gottron III, L. N. Virgin, and B. B. Yellen, Lab on a Chip **10**, 2108 (2010).

[5] B. B. Yellen and L. N. Virgin, Phys. Rev. E **80**, 011402 (2009).

[6] B. B. Yellen, R. M. Erb, H. S. Son, R. Hewlin, H. Shang, and G. U. Lee, Lab on a Chip **7**, 1681 (2007).

[7] A. R. Kose, B. Fischer, L. Mao, and H. Koser, Proc. Natl. Acad. Sci. U.S.A. **106**, 21478 (2009).

[8] B. H. McNaughton, K. A. Kehbein, J. N. Anker, and R. Kopelman, J. Phys. Chem. B **110**, 18958 (2006).

[9] A. Soba, P. Tierno, T. M. Fischer, and F. Sagues, Phys. Rev. E **77**, 060401 (2008).

[10] P. Tierno, S. V. Reddy, J. Yuan, T. H. Johansen, and T. M. Fischer, J. Phys. Chem. B **111**, 13479 (2007).

[11] P. Tierno, F. Sagues, T. H. Johansen, and T. M. Fischer, Phys. Chem. Chem. Phys. **11**, 9615 (2009).

[12] N. G. Green and H. Morgan, J. Phys. D **30**, L41 (1997).

[13] K. Xiao and D. G. Grier, Phys. Rev. Lett. **104**, 028302 (2010).

[14] M. Pelton, K. Ladavac, and D. G. Grier, Phys. Rev. E **70**, 031108 (2004).

[15] Y. Roichman, V. Wong, and D. G. Grier, Phys. Rev. E **75**, 011407 (2007).

[16] P. T. Korda, M. B. Taylor, and D. G. Grier, Phys. Rev. Lett. **89**, 128301 (2002).

[17] K. Ladavac, K. Kasza, and D. G. Grier, Phys. Rev. E **70**, 010901 (2004).

[18] A. Gopinathan and D. G. Grier, Phys. Rev. Lett. **92**, 130602 (2004).

[19] M. Madou, *Fundamentals of Microfabrication: The Science of Miniaturization*, 2nd ed. (CRC Press, Boca Raton, FL, 2002).

[20] O. Hellwig, T. Hauet, T. Thomson, E. Dobisz, J. D. Risner-Jamtgaard, D. Yaney, B. D. Terris, and E. E. Fullerton, Appl. Phys. Lett. **95**, 232505 (2009).

[21] See Supplemental Material at http://link.aps.org/supplemental/10.1103/PhysRevE.84.011403 for videos illustrating bead trajectories.

[22] Y. Ran, J. M. Fu, G. Y. Sheng, R. Beckett, and B. T. Hart, Chemosphere **41**, 33 (2000).

[23] S. Anger, K. Caldwell, H. Niehus, and R. H. Muller, Pharm. Res. **16**, 1743 (1999).

[24] M. Baalousha, F. V. D. Kammer, M. Motelica-Heino, and H. S. Hilal, J. Chromatogr. A **1104**, 272 (2006).

[25] S. L. Brimhall, M. N. Myers, K. D. Caldwell, and J. C. Giddings, J. Polym. Sci. **22**, 339 (1984).

[26] P. Reschiglian, A. Zattoni, B. Roda, E. Michelini, and A. Roda, Trends Biotechnol. **23**, 475 (2005).